

# Onboard Neuromorphic Split Computing via Optical Links for LEO Remote Sensing

Zihang Song *Member, IEEE*, Petar Popovski *Fellow, IEEE*

**Abstract**—Low Earth orbit (LEO) satellite constellations increasingly require onboard intelligence under strict power and communication constraints. This paper proposes a neuromorphic split computing framework tailored for hierarchical LEO systems, where edge satellites perform event-driven sensing using dynamic vision sensors (DVS) and lightweight spiking neural network (SNN) encoders, while core satellites conduct inference using a powerful SNN decoder. A learned spike mapping scheme enables direct transmission over optical inter-satellite links (OISLs) without conventional modulation overhead. Experimental results on synthetic aerial scene classification demonstrate that the proposed architecture achieves accuracy on par with modern large vision-based pipelines, while offering energy efficiency comparable to that of existing lightweight implementations. These findings highlight the potential of neuromorphic computing for energy-efficient inter-satellite split computing in LEO remote sensing missions.

**Index Terms**—Neuromorphic Computing, Spiking Neural Networks, Split Computing, Optical Inter-Satellite Links, Remote Sensing, Energy Efficiency

## I. INTRODUCTION

Split computing is emerging as a practical solution for intelligent remote sensing, particularly in low Earth orbit (LEO) constellations [1]. As shown in Fig. 1, LEO constellations often consist of satellites with heterogeneous capabilities, where smaller, power-constrained satellites (edge nodes) perform sensing and lightweight preprocessing, and larger or better-equipped satellites (core nodes) take on complex inference and selective downlink. Optical inter-satellite links (OISLs) provide stable, high-throughput channels that support efficient data exchange with minimal communication overhead [2].

The high-resolution sensory data collected at edge nodes imposes significant demands on both onboard preprocessing and downstream inference at core nodes. A key challenge lies in meeting these demands under strict power constraints. Recent missions have demonstrated real-time onboard preprocessing using lightweight convolutional neural networks (CNNs) and quantized models, but their accuracy and scalability remain limited

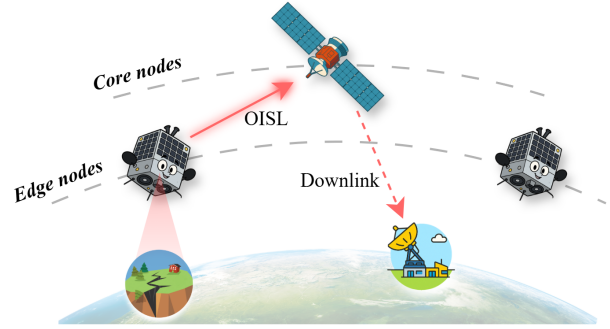


Fig. 1. Conceptual illustration of the LEO hierarchical satellite architecture. Edge nodes are responsible for sensing and preliminary processing, while core nodes aggregate data via optical inter-satellite links (OISLs), perform higher-level tasks, and manage downlink to ground stations.

by tight energy budgets [3]–[5]. For instance, CubeSat-class satellites typically operate within a few watts [6], far below the 50–100 W required by high-performance vision models [7], which makes such models unsuitable for onboard deployment.

*Neuromorphic sensing and computing*, inspired by biological neural systems [8], has emerged as a promising paradigm for ultra-efficient data acquisition and processing [9]. Neuromorphic sensors are event-driven devices that respond only to changes occurring in the observed scene. As a result, they generate less redundant data and consume less power than conventional frame-based sensors. The sparse, spike-based output produced by these sensors is naturally suited for processing by spiking neural networks (SNNs), which propagate temporal spike trains that emulate the behavior of biological neurons [10]. When implemented on specialized digital or mixed-signal hardware, such systems can achieve ultra-low power consumption, with energy usage as low as a few picojoules per spike [11].

Recent space missions have demonstrated the feasibility of neuromorphic sensing and processing in orbit. Neuromorphic sensors have been deployed for high-dynamic-range visual tasks [12], [13], while neuromorphic processors have enabled onboard inference under constrained power budgets [14]. However, these efforts have primarily focused on isolated components and do not account for the functional heterogeneity within LEO constellations. In particular, the potential for coordinated processing between sensing-oriented edge satellites and

The work was supported by Horizon Europe Marie Skłodowska-Curie Action (MSCA) Postdoc Fellowships with grant No. 101206861.

Z. Song (zihang.song@kcl.ac.uk) is with the Center for Intelligent Information Processing Systems (CIIPS), Department of Engineering, King's College London, WC2R 2LS London, UK. P. Popovski (petarp@es.aau.dk) is with the Connectivity Section, Department of Electronic Systems, Aalborg University, 9220 Aalborg, Denmark.

compute-capable core satellites, interconnected via stable OISLs, remains largely unexplored.

In this work, we propose a neuromorphic-native split computing architecture tailored for hierarchical LEO constellations. The main contributions are as follows:

- A neuromorphic split computing architecture is introduced, in which edge nodes perform event-driven sensing using dynamic vision sensors (DVS) and encode data via a lightweight SNN, while core nodes carry out fine-grained inference and manage selective downlink using a high-capacity yet power-efficient SNN decoder.
- In the proposed design, spike-based neuromorphic signals are transmitted directly over OISLs without conventional modulation. To support this, a learned mechanism reorganizes the spike temporal patterns that preserve spike integrity while optimizing optical channel compatibility.
- The proposed architecture is validated through a classification task on synthetic aerial scenes and a stochastic optical channel. The results show that it achieves accuracy on par with modern vision model-based pipelines while reducing encoder and decoder energy consumption by over  $10\times$  and  $2.5\times$ , respectively. The overall energy efficiency is comparable to that of existing lightweight CNN implementations.

## II. SYSTEM OVERVIEW

### A. Optical Inter-Satellite Link

We model the OISL as a free-space optical (FSO) link, following the system studied in [15]. The transmitted signal is defined by a binary sequence  $\mathbf{s} = [s_1, s_2, \dots, s_N] \in \{0, 1\}^N$ , where each bit  $s_n$  modulates the intensity of the optical carrier using on-off keying (OOK) as

$$x[n] = \begin{cases} P_{\text{on}}, & \text{if } s_n = 1, \\ 0, & \text{if } s_n = 0, \end{cases} \quad (1)$$

where  $P_{\text{on}}$  is the optical power level used to transmit a logical '1'.

The received signal  $y[n]$  is expressed as [15]

$$y[n] = RG_o L_{\text{FS}} x[n] e^{-G_e[n]} + w[n], \quad (2)$$

where  $e[n] \sim \chi^2(4, \sigma^2)$  is a statistical abstraction that models the residual pointing error per bit after standard beam-tracking technique [16],  $R$  is the photodetector responsivity,  $G_o$  is the transmitter optical amplifier gain,  $L_{\text{FS}}$  is the deterministic free-space path loss,  $G$  is the pointing sensitivity of the received power to pointing errors, and  $w[n] \sim \mathcal{N}(0, \sigma_w^2)$  is additive Gaussian noise with zero mean and variance

$$\sigma_w^2 = \sigma_0^2 + kRG_o L_{\text{FS}} x[n] e^{-G_e[n]}, \quad (3)$$

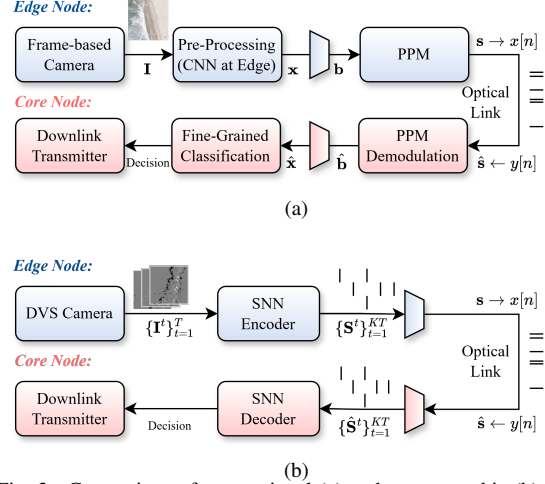


Fig. 2. Comparison of conventional (a) and neuromorphic (b) remote sensing pipelines in a hierarchical satellite system.

where  $\sigma_0^2$  is the signal-independent noise power, and  $k$  captures the proportionality of signal-dependent noise.

The receiver applies a hard-thresholding decision

$$\hat{s}_n = \begin{cases} 1, & \text{if } y[n] > \theta, \\ 0, & \text{otherwise,} \end{cases} \quad (4)$$

where  $\theta = \frac{1}{2}RG_o P_{\text{on}} L_{\text{FS}} (1 + G\sigma^2)^{-2}$  approximates the expected midpoint of the received signal under pointing error fading. This yields the estimated bit sequence  $\hat{\mathbf{s}} = [\hat{s}_1, \hat{s}_2, \dots, \hat{s}_N] \in \{0, 1\}^N$ .

### B. Conventional Split Computing Pipeline

In the conventional pipeline, as shown in Fig. 2(a), the edge node is equipped with a frame-based camera. The sensed image is denoted by  $\mathbf{I} \in \mathbb{R}^{C \times H \times W}$ , where  $C$  is the number of channels,  $H$  and  $W$  represent the spatial resolution of the sensor.

A lightweight convolutional neural network (CNN) is deployed onboard to perform encoding, yielding a compact feature representation  $\mathbf{x} \in \mathbb{R}^D$ . This feature vector is then quantized to  $q$  bits per entry and serialized into a bitstream  $\mathbf{b} \in \{0, 1\}^{Dq}$ .

For bandwidth efficiency and auto-synchronization, the bitstream  $\mathbf{b}$  undergoes pulse position modulation (PPM). Specifically,  $\mathbf{b}$  is segmented into  $N' = \lfloor Nq/\log_2 M \rfloor$  consecutive chunks of  $\log_2 M$  bits, each mapped to a PPM symbol index  $m_i \in \{0, 1, \dots, M-1\}$ , where  $i = 1, \dots, N'$ . Then the modulated sequence  $\mathbf{s} \in \{0, 1\}^N$  is generated with  $N = N'M$ , such that

$$s_{\ell M + m_\ell} = 1, \quad \text{and} \quad s_n = 0 \quad \text{for } n \neq \ell M + m_\ell. \quad (5)$$

Then  $\mathbf{s}$  is transmitted as per Section II-A.

At the core node, the received data  $\hat{\mathbf{s}}$  is demodulated and deserialized to recover the feature representation  $\hat{\mathbf{x}} \in \mathbb{R}^D$ . A more powerful inference model, such as a deep CNN or lightweight vision transformer, is then applied

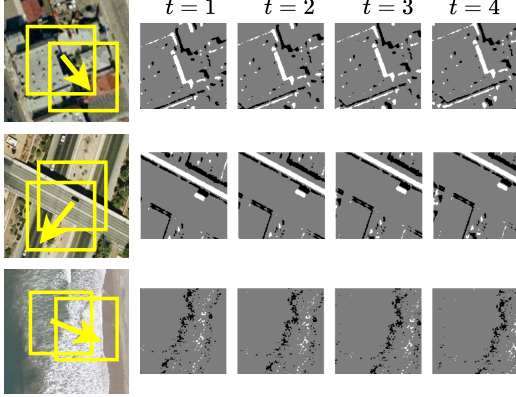


Fig. 3. Spatiotemporal event streams generated from representative satellite scenes using a DVS-based sensor. Each column shows a region of interest, with corresponding event frames over five time steps ( $t = 1$  to  $t = 4$ ).

to perform fine-grained classification or detection. The output (e.g., class labels and probability distribution) is downlinked to the ground station.

### III. NEUROMORPHIC SPLIT COMPUTING VIA OPTICAL INTER-SATELLITE LINK

#### A. System Dataflow

In the proposed system, the edge node adopts a DVS camera, which outputs an asynchronous stream of sparse spatiotemporal events. Each event is represented as a tuple  $(h, w, p, \tau)$ , where  $(h, w)$  is the pixel location,  $p \in \{-1, +1\}$  indicates a brightness change polarity, and  $\tau$  is the time. For visualization and compatibility with spike-based neural processing, we accumulate events over short time intervals to form a sequence of sparse dual-polarity event frames  $\{\mathbf{I}^t\}_{t=1}^T$ , with  $\mathbf{I}^t \in \{-1, 0, 1\}^{H \times W}$ . As shown in Fig. 3,  $I_{h,w}^t = \pm 1$  denotes a significant brightness change at pixel  $(h, w)$  during the  $t$ -th time bin, while 0 indicates no event.

These time-binned events are directly processed by an encoder SNN, which extracts spatiotemporal features through event-driven computation. The basic component of SNNs is the *leaky integrate-and-fire* (LIF) neuron, which integrates input currents over time and emits a spike when the membrane potential exceeds a threshold, described as

$$\begin{aligned} V_-^t &= \beta V_+^{t-1} + \mathcal{I}^t, \\ O^t &= \Theta(V_-^t - V_{\text{thresh}}), \\ V_+^t &= V_-^t(1 - O^t), \end{aligned} \quad (6)$$

where  $V_-^t, V_+^t \in \mathbb{R}$  denote membrane potentials before and after spike emission,  $\mathcal{I}^t$  is the input current,  $\beta$  is the decay factor, and  $O^t$  is the binary spike output.

The encoder SNN processes the input sequence  $\{\mathbf{I}^t\}_{t=1}^T$  and outputs a spike tensor  $\mathbf{X}^t \in \{0, 1\}^{L \times D}$  at each time step, where  $L$  is the number of embeddings and  $D$  the embedding dimension.

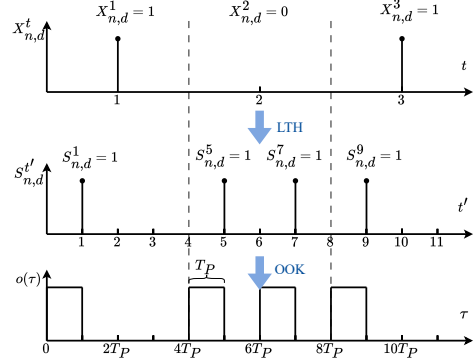


Fig. 4. Illustration of the learned time-hopping (LTH) encoding process in the proposed neuromorphic split computing system.

Due to the temporal sparsity of  $\{\mathbf{X}^t\}$ , direct transmission over an optical link using on-off keying (OOK) can lead to poor bandwidth utilization and synchronization difficulties. To address this, we employ a *learned time-hopping* (LTH) encoding scheme [17], integrated into the final layer of the encoder SNN. Each spike  $X_{l,d}^t$  is expanded into a temporal pattern  $\{S_{l,d}^{t'}\}_{t'=(t-1)K+1}^{tK}$  across  $K$  slots, forming the time-expanded sequence  $\{\mathbf{S}^t\}_{t=1}^{KT}$ , with  $\mathbf{S}^t \in \{0, 1\}^{L \times D}$ .

The binary sequence is serialized into a vector  $\mathbf{s} \in \{0, 1\}^{KTDL}$  and transmitted over the optical channel as discussed in Section II-A. At the core node, the received signal  $\hat{\mathbf{s}}$  is deserialized to reconstruct the spike sequence  $\{\hat{\mathbf{S}}^t\}_{t=1}^{KT}$ . This is processed by a decoder SNN, which integrates spikes to infer a task-specific output, such as object classification or event detection.

#### B. Edge Node SNN Encoder

We adopt the Spiking Token Mixer (STMixer) architecture [18] as the encoder backbone due to its lightweight design and full compatibility with the event-driven nature of DVS data. STMixer effectively extracts global features through two types of linear operations: token (inter-patch) mixing and channel (inter-dimension) mixing, both implemented in a spike-based manner.

As shown in Fig. 5(a), at each time step  $t$ , the DVS input  $\mathbf{I}^t$  is partitioned into a token sequence  $\tilde{\mathbf{X}}^t \in \{0, 1\}^{N \times D}$  via a spiking patch splitting module [19], where  $N$  is the number of tokens and  $D$  is the token dimension.

Each STMixer block performs token mixing followed by channel mixing. The token mixing operation is formulated as:

$$\mathbf{X}^t = \text{LIF}^t \left( \mathbf{W}_{\text{TM}} \text{LIF}^t \left( \text{BN}(\tilde{\mathbf{X}}^t \mathbf{W}_V) \right) \right), \quad (7)$$

where  $\text{BN}(\cdot)$  denotes batch normalization,  $\text{LIF}^t(\cdot)$  denotes leaky integrate-and-fire activation at time  $t$ ,  $\mathbf{W}_V \in \mathbb{R}^{D \times D}$  projects features into a value space, and  $\mathbf{W}_{\text{TM}} \in \mathbb{R}^{N \times N}$  mixes tokens across spatial positions.

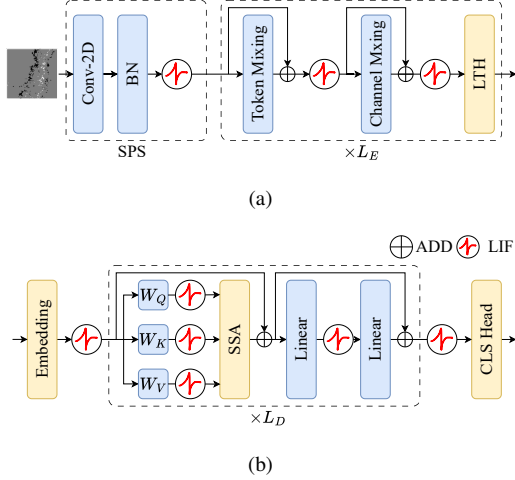


Fig. 5. Network architecture of (a) the edge encoder based on STMixer with LTH output, and (b) the core decoder based on SViT.

Subsequently, channel mixing is applied as:

$$\mathbf{X}^t \leftarrow \text{LIF}^t(\text{BN}(\mathbf{X}^t \mathbf{W}_{\text{CM}} + \epsilon_{\text{CM}})), \quad (8)$$

where  $\mathbf{W}_{\text{CM}} \in \mathbb{R}^{D \times D}$  and  $\epsilon_{\text{CM}} \in \mathbb{R}^D$  are trainable weights and biases. Residual connections are applied after each mixing step to preserve feature integrity.

After  $L_E$  STMixer layers, the final output sequence  $\{\mathbf{X}^t\}_{t=1}^T$ , with  $\mathbf{X}^t \in \{0, 1\}^{L \times D}$ , is passed to an LTH layer. This layer expands each binary spike  $X_{l,d}^t$  into a temporal pattern over  $K$  slots. Specifically, each  $(l, d)$ -th neuron is associated with a trainable embedding  $e_{l,d} \in \mathbb{R}^K$ , and the expanded spike sequence is computed as:

$$S_{l,d}^{(t-1)K+k} = \Theta(W_L(X_{l,d}^t[k] + \epsilon_{l,d}[k])), k = 1, \dots, K, \quad (9)$$

where  $W_L$  is a linear mapping and  $\epsilon_{l,d} \in \mathbb{R}^K$  is a learned bias vector. This allows both  $X_{l,d}^t = 0$  and 1 to emit flexible, content-dependent spike patterns.

### C. Core Node SNN Decoder

At the core node, we deploy a *Spiking Vision Transformer (SViT)* for high-accuracy inference, implemented on a hybrid analog-digital platform for energy-efficient processing. SViT incorporates inter-token attention using event-driven multi-head self-attention mechanisms.

The de-serialized sequence  $\{\hat{\mathbf{S}}^t\}_{t=1}^{KT}$  received from the optical channel is real-valued due to channel distortions. Each timestep's input is embedded as

$$\mathbf{E}_{(0)}^t = \text{LIF}^t(\hat{\mathbf{S}}^t \mathbf{W}_E + \mathbf{P}_E), \quad (10)$$

where  $\mathbf{W}_E \in \mathbb{R}^{D \times D_E}$  is a trainable projection matrix and  $\mathbf{P}_E \in \mathbb{R}^{L \times D_E}$  provides positional encoding. The embedded spike matrix  $\mathbf{E}_{(0)}^t$  is processed by a stack of  $L_D$  SViT layers, producing  $\mathbf{E}_{(1)}^t, \dots, \mathbf{E}_{(L_D)}^t \in \{0, 1\}^{L \times D_E}$ .

As detailed in Algorithm 1, each SViT layer implements a spiking multi-head self-attention (MHSA)

block followed by a spiking feedforward network. The attention is based on stochastic spiking attention (SSA) [20], which replaces costly dot-product operations with lightweight binary logic (e.g., AND) and Bernoulli sampling over discrete QKV representations. This preserves the event-driven sparsity throughout computation and is efficiently executed on the energy-optimized hardware platform described in [21].

### Algorithm 1 Spiking Vision Transformer (SViT) Layer

```

1: Input:  $\mathbf{E}_{(n_L-1)}^t \in \{0, 1\}^{L \times D_E}$ 
2: Output:  $\mathbf{E}_{(n_L)}^t \in \{0, 1\}^{L \times D_E}$ 
3: for each head  $h = 1, \dots, N_H$  do in parallel:
4:    $\mathbf{Q}^t \leftarrow \text{LIF}^t(\mathbf{E}_{(n_L-1)}^t \mathbf{W}_Q^h)$ 
5:    $\mathbf{K}^t \leftarrow \text{LIF}^t(\mathbf{E}_{(n_L-1)}^t \mathbf{W}_K^h)$ 
6:    $\mathbf{V}^t \leftarrow \text{LIF}^t(\mathbf{E}_{(n_L-1)}^t \mathbf{W}_V^h)$ 
7:   for each pair  $(\ell, \ell')$  in  $L \times L$  do
8:      $M_{\ell, \ell'}^t \sim \text{Bern}\left(\frac{1}{D_K} \sum_d Q_{\ell, d}^t \wedge K_{\ell', d}^t\right)$ 
9:   end for
10:  for each  $(\ell, d)$  in  $L \times D_K$  do
11:     $A_{h, d, \ell}^t \sim \text{Bern}\left(\frac{1}{L} \sum_{\ell'} M_{\ell, \ell'}^t \wedge V_{d, \ell'}^t\right)$ 
12:  end for
13: end for
14:  $\mathbf{A}^t = [\mathbf{A}_1^t, \dots, \mathbf{A}_{N_H}^t] \in \{0, 1\}^{L \times D_E}$ 
15:  $\mathbf{E}_{(n_L)}^t \leftarrow \text{LIF}^t(\text{LIF}^t(\mathbf{A}^t \mathbf{W}_1 + \epsilon_1) \mathbf{W}_2 + \epsilon_2)$ 

```

The final layer outputs  $\{\mathbf{E}_{(L_D)}^t\}_{t=1}^{KT}$  are pooled across tokens at each timestep to obtain  $\mathbf{e}^t = \text{Pool}(\mathbf{E}_{(L_D)}^t) \in \mathbb{R}^{D_E}$ . A linear classification head  $\mathbf{W}_{\text{cls}} \in \mathbb{R}^{D_E \times C}$  maps each pooled embedding  $\mathbf{e}^t \in \mathbb{R}^{D_E}$  to class logits, and the final decision vector is computed via temporal averaging:

$$\mathbf{z} = \frac{1}{KT} \sum_{t=1}^{KT} \mathbf{e}^t \mathbf{W}_{\text{cls}}, \quad \mathbf{z} \in \mathbb{R}^C, \quad (11)$$

where  $C$  is the number of target classes.

### D. End-to-End Training

The system is trained end-to-end by jointly optimizing the STMixer encoder and SViT decoder across a differentiable model of the optical channel. The transmitted spike sequences are subject to channel impairments, modeled with the following parameters: photodetector responsivity  $R \sim \mathcal{U}(0.6, 0.9)$  A/W, optical amplifier gain  $G_o \sim \mathcal{U}(20, 40)$  dB, free-space loss  $L_{\text{FS}} \sim \mathcal{U}(10, 15)$  dB, fixed gain  $G = 10^6$ , and noise variance  $\sigma^2 \sim \mathcal{U}(0, 5 \times 10^{-7})$ .

Non-differentiable components such as the LIF activation and Bernoulli sampling are handled using surrogate gradient techniques. The LTH parameters are optimized jointly via the straight-through estimator [22].

The cross-entropy loss

$$\mathcal{L} = \text{CrossEntropy}(\text{Softmax}(\mathbf{z}), \mathbf{z}_{\text{true}}) \quad (12)$$

is minimized over the temporally integrated logits  $\mathbf{z} \in \mathbb{R}^C$  using backpropagation through time.



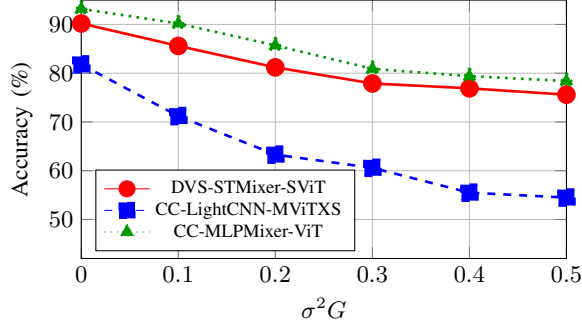


Fig. 6. Classification accuracy versus variance of the radial pointing error.

#### IV. NUMERICAL SIMULATIONS

##### A. Setup

We evaluate the proposed neuromorphic split computing system under realistic remote sensing conditions. The *UC-Merced* land use dataset [23] is used, which consists of 2100 RGB aerial images across 21 land use classes, each at a resolution of  $256 \times 256$ . To simulate DVS data, a  $128 \times 128$  region is randomly cropped from each image and progressively shifted in one direction to generate a synthetic motion sequence. This sequence is converted into a spatiotemporal event stream with  $T = 20$  time steps using the *Video-to-Event* framework [24] (see Fig. 3). The dataset is split evenly into 50% training and 50% evaluation subsets.

The encoder and decoder are trained jointly using the Adam optimizer. The encoder adopts a patch size of  $16 \times 16$  pixels, with  $L_E = 3$  STMixer layers, token dimension  $D = 64$ , and time expansion factor  $K = 4$ . The decoder uses  $L_D = 8$  SViT layers with embedding size  $D_E = 768$  and  $N_H = 16$  attention heads.

During evaluation, the FSO link was configured with a photodetector responsivity of  $R = 0.8$  A/W, an optical amplifier gain of  $G_o = 30$  dB, and a free-space path loss of  $L_{FS} = 14.3$  dB.

**Baselines:** The proposed implementation is referred to as *DVS-STMixer-SViT*. We compare it against two conventional-camera (CC) baselines, both using 8-bit quantization for fairness and hardware compatibility.

(i) *CC-LightCNN-MViTXS*: This baseline uses a CC with a lightweight MobileNetV2-0.1 $\times$  encoder at the edge (75K parameters,  $\sim 7$  MFLOPs per frame) [25], consistent with CubeSat constraints (e.g.,  $\Phi$ -Sat-1). The core node employs a MobileViT-XS decoder (2.7M parameters,  $\sim 640$  MFLOPs) [26].

(ii) *CC-MLPMixer-ViT*: This baseline uses a non-neuromorphic MLP Mixer encoder [27] at the edge and a conventional non-neuromorphic ViT decoder at the core, scaled to align with the size of the STMixer and SViT, respectively.

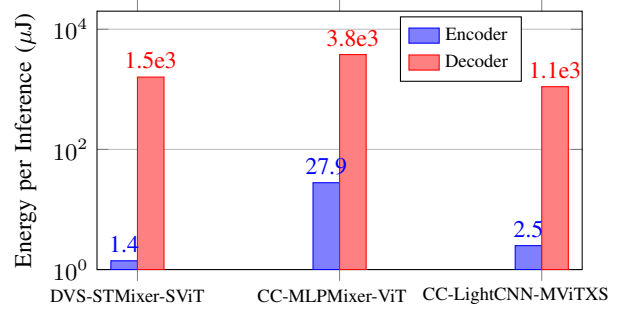


Fig. 7. Encoder and decoder energy consumption per inference for each system.

##### B. Results

1) *Classification Accuracy under Pointing Error*: We evaluate the robustness of the proposed DVS-STMixer-SViT system to radial pointing errors, quantified by the normalized pointing error variance  $\sigma^2 G$ , following the model in [15]. Figure 6 presents the classification accuracy over a range of  $\sigma^2 G \in [0, 0.5]$ .

Among all models, CC-MLPMixer-ViT shows the most stable performance. The proposed DVS-STMixer-SViT, however, tracks closely across the entire range and consistently outperforms CC-LightCNN-MViTXS. At zero pointing error ( $\sigma^2 G = 0$ ), DVS-STMixer-SViT achieves 90.2% accuracy and degrades gracefully to 75.6% at  $\sigma^2 G = 0.5$ , remaining within a narrow margin of CC-MLPMixer-ViT throughout. In contrast, CC-LightCNN-MViTXS peaks at 81.8% and drops steeply to nearly 55% under severe misalignment.

2) *Energy Consumption*: We estimate the energy consumption of the proposed DVS-STMixer-SViT system and the two baselines. The analysis accounts for all computational and memory access operations, following the methodology in [28] and the energy table in [29].

As shown in Fig. 7, the proposed DVS-STMixer-SViT achieves the lowest energy consumption across both encoder and decoder. The STMixer encoder consumes only 1.4  $\mu J$  per inference, significantly lower than its non-neuromorphic counterpart, MLP Mixer (27.9  $\mu J$ ), and even below the lightweight LightCNN (2.5  $\mu J$ ). This makes it well-suited for deployment on power-constrained edge nodes, combining high encoding capacity with minimal energy use. On the core node side, the SViT decoder consumes 1.5 mJ per inference, which is 2.5 $\times$  lower than the non-neuromorphic counterpart ViT (3.8 mJ) and comparable to the compact MViTXS decoder (1.1 mJ). These results demonstrate that the proposed neuromorphic split computing system offers a favorable balance between accuracy comparable to large transformer-based baselines while maintaining energy efficiency on par with highly compact CNNs, which makes it particularly suitable for deployment in power-constrained satellite environments.

## V. CONCLUSION

This work proposed a neuromorphic split computing architecture for LEO satellite constellations. The system integrates a lightweight spiking token mixer encoder at the edge, a spiking vision transformer at the core, and a learned time-hopping scheme that enables direct spike-based optical transmission without conventional modulation. Simulation results on a representative remote sensing task showed that the architecture achieves classification accuracy on par with Transformer-based pipelines, while reducing energy consumption by up to  $10\times$  at the encoder and  $2.5\times$  at the decoder, which are comparable to existing lightweight CNN-based implementations. Future work will explore improvements in spike-based coding efficiency, transmission-aware learning strategies, and task-oriented optimization for broader downstream applications under resource constraints.

## REFERENCES

- [1] Y. Shi, J. Zhu, C. Jiang, L. Kuang, and K. B. Letaief, "Satellite edge artificial intelligence with large models: Architectures and technologies," *arXiv preprint arXiv:2504.01676*, 2025.
- [2] M. M. Gost, I. Leyva-Mayorga, A. Pérez-Neira, M. Á. Vázquez, B. Soret, and M. Moretti, "Edge computing and communication for energy-efficient earth surveillance with LEO satellites," in *2022 IEEE Int. Conf. Commun. Workshops (ICC Workshops)*. IEEE, 2022, pp. 556–561.
- [3] G. Giuffrida, L. Fanucci, G. Meoni, M. Batič, L. Buckley, A. Dunne, C. van Dijk, M. Esposito, J. Hefe, N. Vercruyssen, G. Furano, M. Pastena, and J. Aschbacher, "The  $\Phi$ -Sat-1 mission: The first on-board deep neural network demonstrator for satellite earth observation," *IEEE Trans. Geosci. Remote Sens.*, vol. 60, pp. 1–14, 2022.
- [4] M. M. C. Muñoz, F. Deconinck, J. B. Ars, N. Melega, C. Pirat, B. J. Soto, A. Dunne, L. Buckley, J. R. Cañas, G. Benelli *et al.*, "MANTIS, a 12U smallsat mission taking advantage of super-resolution and artificial intelligence for high-resolution imagery," in *Proc. Small Sat. Conf.*, 2024.
- [5] A. M. Wijata, T. Lakota, M. Cwiek, B. Ruszczak, M. Gumiela, L. Tulczyjew, A. Bartoszek, N. Longépé, K. Smykala, and J. Nalepa, "Intuition-1: Toward in-orbit bare soil detection using spectral vegetation indices," in *IGARSS 2024 - 2024 IEEE Int. Geosci. Remote Sens. Symp.*, 2024, pp. 1708–1712.
- [6] S. S. Arnold, R. Nuzzaci, and A. Gordon-Ross, "Energy budgeting for cubesats with an integrated FPGA," in *2012 IEEE Aerosp. Conf.*. IEEE, 2012, pp. 1–14.
- [7] T.-D. Le, V. N. Ha, T. T. Nguyen, G. Eappen, P. Thiruvassagam, L. M. Garces-Socarras, H.-f. Chou, J. L. Gonzalez-Rios, J. C. Merlano-Duncan, and S. Chatzinotas, "Onboard satellite image classification for earth observation: A comparative study of vit models," *arXiv preprint arXiv:2409.03901*, 2024.
- [8] C. Mead, "Neuromorphic electronic systems," *Proc. IEEE*, vol. 78, no. 10, pp. 1629–1636, 1990.
- [9] Z. Song, O. Simeone, and B. Rajendran, "Neuromorphic in-context learning for energy-efficient MIMO symbol detection," in *2024 IEEE 25th Int. Workshop Signal Process. Adv. Wireless Commun. (SPAWC)*, 2024, pp. 1–5.
- [10] A. Tavanaei, M. Ghodrati, S. R. Kheradpisheh, T. Masquelier, and A. Maida, "Deep learning in spiking neural networks," *Neural Netw.*, vol. 111, pp. 47–63, 2019.
- [11] M. Davies, N. Srinivasa, T.-H. Lin, G. Chinya, Y. Cao, S. H. Choday, G. Dimou, P. Joshi, N. Imam, S. Jain *et al.*, "Loihi: A neuromorphic manycore processor with on-chip learning," *IEEE Micro*, vol. 38, no. 1, pp. 82–99, 2018.
- [12] I. U. N. Laboratory, "Falcon neuro: First demonstration of event-based sensing in space," in *International Astronautical Congress*, 2022.
- [13] Sidus Space, "Sidus space and Lulav space partner to launch event-based star tracker on June SpaceX mission," <https://investors.sidus-space.com/news-events/press-releases/detail/113/sidus-space-and-lulav-space-partner-to-launch-event-based>, Jul. 2023.
- [14] N. A. R. Center, "TechEdSat-13: On-orbit demonstration of neuromorphic processors in cubesats," *NASA Reports*, 2022.
- [15] S. Armon, "Performance of a laser  $\mu$  satellite network with an optical preamplifier," *J. Opt. Soc. Am. A*, vol. 22, no. 4, pp. 708–715, 2005.
- [16] Y. Kaymak, R. Rojas-Cessa, J. Feng, N. Ansari, M. Zhou, and T. Zhang, "A survey on acquisition, tracking, and pointing mechanisms for mobile free-space optical communications," *IEEE Commun. Surv. Tutorials*, vol. 20, no. 2, pp. 1104–1123, 2018.
- [17] J. Chen, N. Skachkovsky, and O. Simeone, "Neuromorphic wireless cognition: Event-driven semantic communications for remote inference," *IEEE Trans. Cogn. Commun. Netw.*, vol. 9, no. 2, pp. 252–265, 2023.
- [18] S. Deng, Y. Wu, K. Du, and S. Gu, "Spiking token mixer: An event-driven friendly former structure for spiking neural networks," *Adv. Neural Inf. Process. Syst.*, vol. 37, pp. 128 825–128 846, 2024.
- [19] Z. Zhou, Y. Zhu, C. He, Y. Wang, S. Yan, Y. Tian, and L. Yuan, "Spikformer: When spiking neural network meets transformer," *arXiv preprint arXiv:2209.15425*, 2022.
- [20] Z. Song, P. Katti, O. Simeone, and B. Rajendran, "Stochastic spiking attention: Accelerating attention with stochastic computing in spiking networks," in *2024 IEEE 6th Int. Conf. AI Circuits Syst. (AICAS)*, 2024, pp. 31–35.
- [21] —, "Xpikeformer: Hybrid analog-digital hardware acceleration for spiking transformers," *IEEE Trans. Very Large Scale Integr. (VLSI) Syst.*, vol. 33, no. 6, pp. 1596–1609, 2025.
- [22] A. Tjandra, S. Sakti, and S. Nakamura, "End-to-end feedback loss in speech chain framework via straight-through estimator," in *ICASSP 2019-2019 IEEE Int. Conf. Acoust. Speech Signal Process. (ICASSP)*. IEEE, 2019, pp. 6281–6285.
- [23] Y. Yang and S. Newsam, "Bag-of-visual-words and spatial extensions for land-use classification," in *Proc. 18th SIGSPATIAL Int. Conf. Advances Geographic Inf. Syst.*, 2010, pp. 270–279.
- [24] Y. Hu, S.-C. Liu, and T. Delbruck, "v2e: From video frames to realistic dvs events," in *Proc. IEEE/CVF Conf. Comput. Vis. Pattern Recognit.*, 2021, pp. 1312–1321.
- [25] M. Sandler, A. Howard, M. Zhu, A. Zhmoginov, and L.-C. Chen, "Mobilenetv2: Inverted residuals and linear bottlenecks," in *Proc. IEEE Conf. Comput. Vis. Pattern Recognit.*, 2018, pp. 4510–4520.
- [26] S. Mehta and M. Rastegari, "MobileViT: Light-weight, general-purpose, and mobile-friendly vision transformer," *arXiv preprint arXiv:2110.02178*, 2021.
- [27] I. O. Tolstikhin, N. Houlsby, A. Kolesnikov, L. Beyer, X. Zhai, T. Unterthiner, J. Yung, A. Steiner, D. Keysers, J. Uszkoreit *et al.*, "MLP-Mixer: An All-MLP architecture for vision," *Adv. Neural Inf. Process. Syst.*, vol. 34, pp. 24 261–24 272, 2021.
- [28] G. Datta, S. Kundu, A. R. Jaiswal, and P. A. Beerel, "ACE-SNN: Algorithm-hardware co-design of energy-efficient & low-latency deep spiking neural networks for 3D image recognition," *Front. Neurosci.*, vol. 16, 2022.
- [29] A. Pedram, S. Richardson, M. Horowitz, S. Galal, and S. Kvatinisky, "Dark memory and accelerator-rich system optimization in the dark silicon era," *IEEE Des. Test*, vol. 34, no. 2, pp. 39–50, 2017.